Acta Materialia 203 (2021) 116508

Contents lists available at ScienceDirect

Acta Materialia

journal homepage: www.elsevier.com/locate/actamat

Probing potential energy landscapes via electron-beam-induced single atom dynamics

O. Dyck[a,*], M. Ziatdinov[a,g], S. Jesse[a], F. Bao[b], A. Yousefzadi Nobakht[c], A. Maksov[a,f], B.G. Sumpter[a], R. Archibald[d], K.J.H. Law[d,e], S.V. Kalinin[a]

[a] Center for Nanophase Materials Sciences, Oak Ridge National Laboratory, Oak Ridge, TN 37831
[b] Department of Mathematics, Florida State University, Tallahassee, FL, 32304
[c] Department of Mechanical, Aerospace, and Biomedical Engineering, The University of Tennessee, Knoxville, TN 37996
[d] Computer Science and Mathematics Division, Oak Ridge National Laboratory, Oak Ridge, TN 37831
[e] Department of Mathematics, University of Manchester, Manchester, UK
[f] Bredesen Center for Interdisciplinary Research and Education, The University of Tennessee, Knoxville, TN 37996
[g] Computational Sciences and Engineering Division, Oak Ridge National Laboratory, Oak Ridge, TN

ARTICLE INFO

Article history:
Received 30 June 2020
Revised 16 October 2020
Accepted 17 November 2020
Available online 22 November 2020

Keywords:
potential energy landscape
atomic dynamics
graphene
scanning transmission electron microscope

ABSTRACT

Structure, bonding, and chemical dynamics of reactions at surfaces and interfaces, and therefore most material properties are intrinsically tied to the energetic landscape in which each atom resides. Here, we demonstrate that a moving atom under electron beam excitation can be used to probe the energy landscape along (confined) step edges, providing information about atomic-scale potentials. The techniques for experimentally exploring atomic potentials holds promise for predictive atom-by-atom fabrication using electron beams.

© 2020 Published by Elsevier Ltd on behalf of Acta Materialia Inc.

1. Introduction

The dynamics of atomic and molecular species on surfaces are inherent for catalysis, phase formation and crystallization, and other heterogeneous processes. Generally, the presence of impurities, extended defects, and step edges strongly influences the chemical binding landscape of the surface, creating preferential paths for atomic transport. The ability to explore and engineer such pathways is instrumental toward the predictive design of functional materials for directed transport and catalysis.

These phenomena have gained new significance in light of advances in scanning transmission electron microscopy (STEM). Observations of bulk- and surface adatom dynamics induced by the electron beam (e-beam) have been reported and this beam control has recently been harnessed to tailor materials at the atomic scale [1–12].

A major challenge of e-beam atomic manipulation in the STEM is understanding the energetic landscape in real experimental environments surrounding an atom of interest and providing a targeted amount of energy and momentum to produce the desired modification. The e-beam in a STEM can produce a wide array of interesting processes [13,14]; however, harnessing and precisely directing the atomic transformations can be difficult. Nevertheless, careful observation and analysis of e-beam-driven events can begin to reveal controllable processes that can then be leveraged in fabrication workflows [2,6]. In the spirit of this endeavor, here we carefully track the evolution of atomic positions during e-beam irradiation and reconstruct the free energy landscape along a confined graphene step edge to within an offset and scale factor. This procedure reveals atomic-level changes in the energy landscape and forms the first step toward uncovering controllable processes that may be used for directed atomic movement.

2. Sample preparation and imaging

A few-layer graphene sample for STEM was prepared from a chemical vapor deposition (CVD)-grown graphene on Cu foil with a protective overcoating of poly(methyl-methacrylate) (PMMA). The PMMA/graphene/Cu was floated on a solution of ammonium persulfate/deionized (DI) water until the Cu foil etched away. The PMMA/graphene was rinsed with DI water to remove the ammonium persulfate residue and the graphene film was transferred to a Protochips™ MEMS-based heater chip. The heater chip with graphene was baked on a hot plate at 150 °C for 15 min. to pro-

* Corresponding author.
E-mail address: dyckoe@ornl.gov (O. Dyck).

https://doi.org/10.1016/j.actamat.2020.116508
1359-6454/© 2020 Published by Elsevier Ltd on behalf of Acta Materialia Inc.

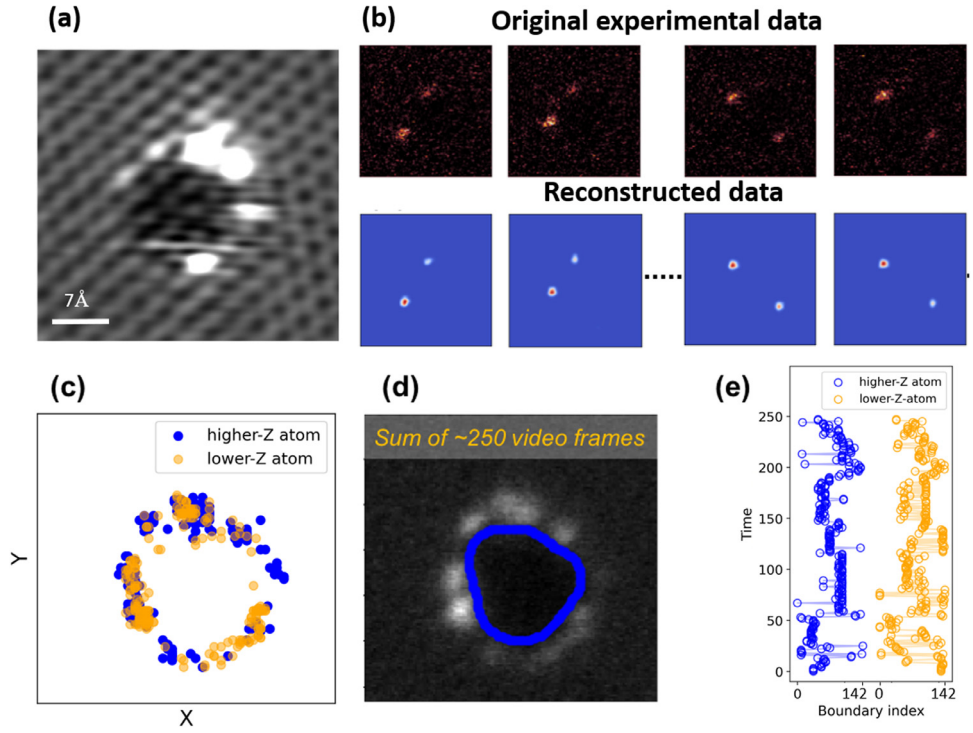

Fig. 1. Deep convolutional autoencoder-based analysis of impurity trajectories along the edge of a graphene hole. (a) HAADF-STEM image of sample configuration where decorating atoms are attached to the step edge of bilayer graphene. To resolve the graphene lattice a slow scan was used. The dynamically moving decorating atoms appear in multiple locations. (b) Representative image frames of the fast-scanned experimental STEM "movie" with two atomic impurities and the output of convolutional de-noising autoencoder for image frames shown. (c) Plot of coordinates of atomic positions for higher-Z and lower-Z atoms extracted for each of 248 movie frames. (d) Average hole contour overlaid onto the image representing a sum of about 248 movie frames. (e) Analysis of decorating atom trajectories along the edge of hole represented as a function of the pixel coordinate along the edge (boundary index).

mote adhesion of the graphene. Acetone was used to dissolve the PMMA protective layer and isopropyl alcohol was used to remove the acetone residue. The sample was then dried in air.

Prior to examination in the STEM, the heater chip was loaded in the sample cartridge and was baked under vacuum at 160 °C for 8 h to remove volatile hydrocarbons. After loading the cartridge in the STEM column, the graphene sample temperature was ramped to 1200 °C at a rate of 1000 °C/ms to clean the graphene and held at this temperature for the duration of the experiment. A Nion UltraSTEM U100 was used for the experiments and was operated at an accelerating voltage of 60 kV to prevent knock-on damage to the graphene lattice. The convergence angle was nominally 30 mrad. A high angle annular dark field (HAADF) detector was used for STEM imaging. A beam current of 67 pA and a 1 µs pixel dwell time were used for an electron dose of 2.5 $\times 10^5$ e/nm^2 per image frame. The pixel size was 15.6 pm. This dwell time results in a fairly fast frame rate (by STEM standards) of 65 ms/frame and was chosen to maximize the time resolution, while at the same time providing enough signal that the brighter atoms could still be detected. This allowed us to capture atomic dynamics that might be hidden by slower scan speeds. It is worth noting that even faster scans would be possible, further boosting the time resolution, if the detector signal could be increased (e.g. through the use of heavier decorating atoms [15]).

In this example, a hole in one layer of a bilayer graphene film was found that had two spurious dopant atoms decorating the step edge. A slow-scanned overview HAADF-STEM image is shown in Fig. 1a, which has been Fourier filtered to reduce noise and clarify the carbon lattice periodicity. The slow scan rate allows sufficient intensity for the graphene lattice to be observed. Due to the mobility of the decorating atoms at the edge of the hole, they move under the beam and appear in multiple locations around the hole in this image. The difference in intensity between the two atoms indicates they are different atomic species, with the brighter one having a higher atomic number [16,17]. Multislice simulations, described in the supplemental information, indicate the elemental identities are likely Si and a first row transition metal, however noise and the dynamic motion of the decorating atoms makes careful intensity analysis prone to error. Because of this uncertainty we will simply refer to them as the "higher-Z" and "lower-Z" atoms. A series of HAADF-STEM images was acquired, exposing the sample to 60 keV e-beam irradiation while simultaneously recording the positions of each atom. During the imaging process, electron impacts impart enough energy to the decorating atoms that they become (momentarily) mobilized and will migrate to a new location. The step edge (or hole edge) acts as an energetic barrier so that the atoms do not migrate away onto and across the graphene surface but continue to move along the edge as they are excited by the e-beam. We note that sample temperature may also contribute to the atomic movements observed, however, the much larger energy transfer from the e-beam is the primary driver. Nevertheless, in our treatment, we rely strictly on observed atomic positions, making no assumptions with regard to the mechanism for motion.

3. Results and discussion

The high level of noise in the experimental series of STEM images (hereafter, referred to as STEM movies) of impurity motion (Fig. 1a) did not allow us to extract the positions of the atomic species in each frame using standard image analysis tools (*e.g.*, median filtering and thresholding). To alleviate this issue, we employed a deep convolutional de-noising autoencoder (CDAE) for processing the raw experimental data [18,19]. The CDAE is a powerful tool for reconstructing missing/corrupted data from images, including images where signal and noise can barely be differenti-

ated by the human eye. We used a CDAE model in which both encoder and decoder parts consist of three convolutional layers separated by a max pooling layer (encoder) and an un-pooling layer (decoder). The CDAE was trained on simulated STEM images corrupted with similar levels of noise as those observed in the experiment. We then applied the trained CDAE to the real STEM movies, which allowed us to reconstruct noisy experimental images (the movie frames) into images with two well-defined atomic impurities of different intensities, e.g., brighter and darker contrast on a uniform background (Fig. 1b). Thus, with the help of CDAE the problem of excessive noise has been reduced to a trivial problem of tracking the motion of two "blobs" of different intensities across the frames of the STEM movies. In two image frames distinct atom locations were indeterminate due to atomic motion during image acquisition. These frames were excluded from the analysis. The extracted positions of the impurity atoms from the STEM movie frames are plotted in Fig. 1c. We then extracted a contour estimate of the hole edges (Fig. 1d) and plotted the impurity atom trajectories as a function of their coordinates along the edge (boundary index) for both the higher-Z and lower-Z atoms (Fig. 1e). The impurity atom dynamics show the characteristics of a telegraph process, where there are long periods of stability with rapid jumps in-between.

The timescale of the pixel dwell time, i.e., microseconds, and the frame acquisition time are effectively macroscale with respect to the femtosecond dynamics and nanosecond impacts from the e-beam, such that the observations of atomic locations are considered to be independent and identically distributed (i.i.d.) realizations from the invariant distribution of the underlying femtoscale process. Here, we have the dynamics of two interacting processes, a lower-Z atom, $S_l(t)$, and a higher-Z atom, $S_h(t)$, which evolve on the torus parameterized by s in [0,1) in units of the circumference of the ring, which is estimated to be 24 - 28 Å. The parameter, s, represents the pixel boundary index shown in Fig 1e (which is based on the pixel density of the data) rescaled for convenience to the interval [0, 1).

Here, we assume the atoms moving along the hole edge can be described by Brownian motion with the overdamped Langevin equation, [20]

$$\frac{dX(t)}{dt} = -\frac{D}{k_B T}\nabla V(X) + \sqrt{2D}\frac{dW}{dt} \tag{1}$$

where $\frac{dX(t)}{dt}$ represents the particle/atom velocity, D is the diffusion constant, k_B is Boltzmann's constant, T is temperature, V(X) is the particle interaction potential, and $\frac{dW}{dt}$ is the standard Wiener process. The invariant distribution of the Langevin diffusion (1), which we call q(x), is proportional to $\exp(-V(x)/k_BT)$. Observations separated by long timescales can therefore be considered independent observations from this target distribution. Operating on this assumption we consider the observations shown in Fig. 1 as i.i.d. drawn from $p(x) = q(x)/Z = \frac{1}{Z}\exp(-V(x)/k_BT)$, where Z is the partition function (the integral $Z = \sum e^{-V(x)/k_BT}$). We will now proceed to recover $U(x) = V(x)/k_BT + \log(Z)$, which is the particle interaction potential, V(x), up to a characteristic energy scaling factor and offset. Note that here we have two interacting particles, thus $x = (s_l, s_h)$ is two dimensional, where the subscripts are used to indicate the lower-Z and higher-Z atoms, respectively. A non-parametric kernel density estimate is used to reconstruct an approximation of the invariant density, $p(s_l, s_h) = \exp(-U(s_l, s_h))$. A Gaussian kernel is used for the non-parametric density reconstruction, as described below, with standard deviation l=0.05, which was chosen "by eye" to produce a smoothly varying potential reconstruction (Fig. 2a). We note that this value translates to ~1.3 Å and therefore corresponds nicely with the characteristic length scale one would expect to find. Fig. 2 shows the marginal reconstructed densities for both s_l and s_h after the full 248 observations.

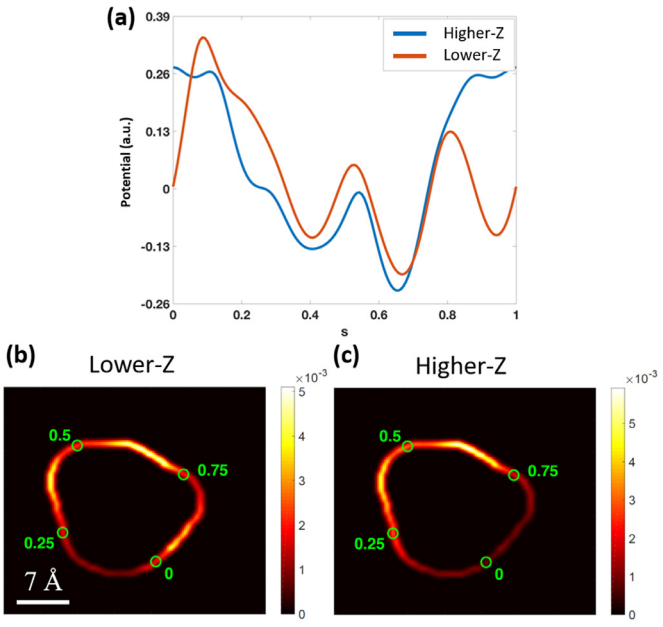

Fig. 2. (a) Potential energy landscape (up to an offset and scaling factor) experienced by atoms along the hole edge and schematic graphene configuration. The parameter, s, represents the position on the hole edge. (b) reconstructed marginal probability density of lower-Z atom, and (c) reconstructed marginal probability density of higher-Z atom, where $p = e^{-U}$. Green circle markers correspond to values of s along the hole edge.

The joint density, which describes correlations between the processes, is shown in Fig. 3.

The non-parametric estimation proceeds by smoothing an empirical distribution through convolution with a Gaussian kernel having bandwidth ℓ

$$K(x;\ell) \propto \exp\{-\frac{1}{2\ell^2}|x|^2\}.$$

In this case, one constructs an empirical measure based on the data points $\{x_i\}_{i=1}^N$ as follows (there is an implicit i.i.d. assumption here)

$$\hat{p}^N(dy) := \frac{1}{N}\sum_{i=1}^{N}\delta_{x_i}(dy),$$

where $\delta_{x_i}(dy)$ is the Dirac delta measured at point x_i of the infinitesimal increment dy, and then a functional approximation of the corresponding density is constructed as follows:

$$\hat{p}_K(x) := \left(K \star \hat{p}^N\right)(x) = \int K(x-y)\hat{p}^N(dy) = \frac{1}{N}\sum_{i=1}^{N}K(x-x_i;\ell)$$

Assuming that K is normalized, one has an estimate for U as well

$$\hat{U}_K(x) := -\log\hat{p}_K(x) \tag{2}$$

The estimator (2) is used to approximate the effective joint potential for the interacting system of higher-Z and lower-Z atoms from the experimental observations $\{x_i\}_{i=1}^N$. In this case $x = (s_l, s_h)$, where $s_l,\ s_h \in [0, 1)$, corresponding to lower-Z and higher-Z atom positions, respectively.

The joint potential arising from the reconstructions of the density $p(s_l, s_h) = \exp(-U(s_l, s_h))$, as described above is shown in Fig. 3. The resulting reconstruction is a dimensionless representation of the potential, scaled by an unknown energy factor, k_BT, (where T incorporates the combined effects of the sample temperature and effective temperature added by the e-beam, which is unknown) and offset by the log of the partition function. The marginal results

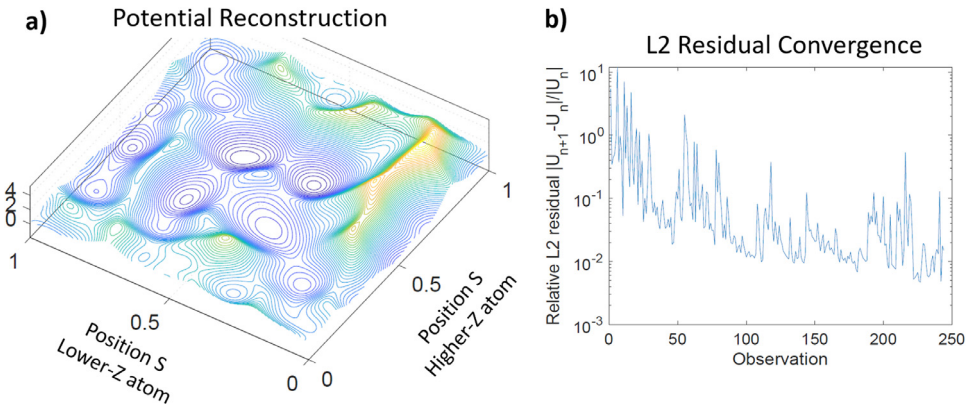

Fig. 3. a) Reconstruction of potential on a torus expanded coordinate system. b) Relative L2 residual as a function of observation number showing the degree of convergence (y axis is on a log scale).

are plotted in Fig. 2. We note that this reconstructed potential, by virtue of the experimental measurement process, includes all influences on the atomic positions whatever they may be. Therefore, it does not necessarily correspond to just the atomic potential of the graphene edge or the atomic potential of the underlying graphene sheet or the atomic potential of the decorating atoms interacting with one another, but all of these (and any other) effects combined in a dynamically varying system.

From this reconstruction we can clearly see low energy valleys which represent locations along the hole edge where interaction between the two atoms is energetically more favorable. In contrast, the peaks represent locations along the hole edge where the atomic interactions are less favorable. For example there is a large energy barrier for the dark atom being close to 0 when the bright atom is close to 1, and the potential energy is low close to the diagonal $S_h = S_l$ corresponding to the decorating atoms stabilizing one another when in directly adjacent positions (the decorating atoms were not observed to occupy the same position concurrent, exactly at $S_h = S_l$). We can begin to get an idea about the relative difficulty of transitioning from one stability point to another and the path of least resistance between them within this expanded coordinate system. These interactions are governed by the edge geometry (edge termination configuration as well as curvature), the location and relative orientation of the underlying graphene sheet, the atomic species of the decorating atoms, sample temperature, and effect of the e-beam. The potential reconstructed in this way, from repeated observations, takes into account all the inherent complexities and dynamic processes in the real-world system. However, this also means the energetic morphology of the potential is not easily separable into the individual components from which it is derived. By way of example, in the reconstruction shown in Fig. 3a we observe two clear energetic wells on either side of the diagonal $S_h = S_l$ mentioned earlier. These wells correspond to the decorating atoms occupying the straighter/flatter regions of the hole but not interacting with each other (i.e. physically separated). The reconstruction gives little indication why this is the case but offers a view into the dynamic system where such features can be identified for further inquiry.

In Fig. 3b we plot the relative L2 residual (on a log scale) calculated for each additional observation. From this metric we observe a strong convergence trend that begins to level off after about 100-150 observations. There may still be a slight downward trend toward the tail (>200) indicating that additional observations could slightly improve the fidelity of the reconstruction, however, the bulk of the convergence occurred within the first 100 observations. This gives indication of the sampling density needed and can be used to evaluate the confidence one should have in the reconstruction.

4. Conclusion

To summarize, here we demonstrate an approach to probe the free energy landscape within a confined region using the dynamic positions of single atoms, which are driven to explore the area through repeated excitations from the scanned e-beam. From the observed atom positions/locations, we are able to reconstruct the energetic landscape up to a scaling factor and offset, which can be used to visualize the relative changes in the surrounding energetic landscape. This study provides a method to describe experimentally observed atom motion and dynamics driven by an e-beam. This procedure is limited to confined systems where the constituents within the system are driven to sample the surrounding neighborhood with a high degree of repetition. This approach helps to uncover atomic dynamics which may enable the discovery of methods for the e-beam to be used as a controllable (or at least a better understood) probe for beam-induced transformations.

Declaration of Competing Interest

The authors declare that they have no known competing financial interests or personal relationships that could have appeared to influence the work reported in this paper.

Acknowledgements

This material is based upon work supported by the U.S. Department of Energy, Office of Science, Basic Energy Sciences, Materials Sciences and Engineering Division (STEM work O.D., S.J., S.V.K.) and was performed at the Oak Ridge National Laboratory's Center for Nanophase Materials Sciences (CNMS), a U.S. Department of Energy, Office of Science User Facility (data analysis M.Z.). This work was also supported by The Alan Turing Institute under the EPSRC grant EP/N510129/1 (K.J.H.L.). We would like to acknowledge the support by the Scientific Discovery through Advanced Computing (SciDAC) funded by the U.S. Department of Energy, Office of Science, Advanced Scientific Computing Research through FASTMath Institutes and partial support by U.S. National Science Foundation under contract DMS-1720222. (F.B.) A.M. acknowledges fellowship support from the UT/ORNL Bredesen Center for Interdisciplinary Research and Graduate Education.

Supplementary materials

Supplementary material associated with this article can be found, in the online version, at doi:10.1016/j.actamat.2020.116508.

References

[1] O. Dyck, S. Kim, E. Jimenez-Izal, A.N. Alexandrova, S.V. Kalinin, S. Jesse, Building Structures Atom by Atom via Electron Beam Manipulation, Small 14 (38) (2018) 1801771.

[2] O. Dyck, S. Kim, S.V. Kalinin, S. Jesse, Placing single atoms in graphene with a scanning transmission electron microscope, Appl. Phys. Lett. 111 (11) (2017) 113104.

[3] O. Dyck, M. Ziatdinov, D.B. Lingerfelt, R.R. Unocic, B.M. Hudak, A.R. Lupini, S. Jesse, S.V. Kalinin, Atom-by-atom fabrication with electron beams, Nat. Rev. Mater. (2019).

[4] C. Su, M. Tripathi, Q.-B. Yan, Z. Wang, Z. Zhang, C. Hofer, H. Wang, L. Basile, G. Su, M. Dong, J.C. Meyer, J. Kotakoski, J. Kong, J.-C. Idrobo, T. Susi, J. Li, Engineering single-atom dynamics with electron irradiation, Science Advances 5 (5) (2019) eaav2252.

[5] T. Susi, D. Kepaptsoglou, Y.-C. Lin, Q.M. Ramasse, J.C. Meyer, K. Suenaga, J. Kotakoski, Towards atomically precise manipulation of 2D nanostructures in the electron microscope, 2D Materials 4 (4) (2017) 042004.

[6] T. Susi, J. Kotakoski, D. Kepaptsoglou, C. Mangler, T.C. Lovejoy, O.L. Krivanek, R. Zan, U. Bangert, P. Ayala, J.C. Meyer, Q. Ramasse, Silicon-Carbon Bond Inversions Driven by 60-keV Electrons in Graphene, Phys. Rev. Lett. 113 (11) (2014) 115501.

[7] T. Susi, J.C. Meyer, J. Kotakoski, Manipulating low-dimensional materials down to the level of single atoms with electron irradiation, Ultramicroscopy 180 (2017) 163–172.

[8] M. Tripathi, A. Mittelberger, N.A. Pike, C. Mangler, J.C. Meyer, M.J. Verstraete, J. Kotakoski, T. Susi, Electron-Beam Manipulation of Silicon Dopants in Graphene, Nano Lett (2018).

[9] S.V. Kalinin, A. Borisevich, S. Jesse, Fire up the atom forge, Nature 539 (7630) (2016) 485–487.

[10] B.M. Hudak, J. Song, H. Sims, M.C. Troparevsky, T.S. Humble, S.T. Pantelides, P.C. Snijders, A.R. Lupini, Directed Atom-by-Atom Assembly of Dopants in Silicon, ACS Nano 12 (6) (2018) 5873–5879.

[11] S. Jesse, Q He., A.R. Lupinin, D. Leonard, M.P. Oxley, O. Ovchinnikov, R.R. Unocic, A. Tselev, M. Fuentes-Cabrera, B.G. Sumpter, S.J. Pennycook, S.V. Kalinin, A.Y. Borisevich, Atomic-Level Sculpting of Crystalline Oxides: Toward Bulk Nanofabrication with Single Atomic Plane Precision, Small (2015) 1.

[12] S. Jesse, B.M. Hudak, E. Zarkadoula, J. Song, A. Maksov, M. Fuentes-Cabrera, P. Ganesh, I. Kravchenko, P.C. Snijders, A.R. Lupini, A.Y. Borisevich, S.V. Kalinin, Direct atomic fabrication and dopant positioning in Si using electron beams with active real-time image-based feedback, Nanotechnology 29 (25) (2018) 255303.

[13] H. Wu, X. Zhao, C. Guan, L.-D. Zhao, J. Wu, D. Song, C. Li, J. Wang, K.P. Loh, T.V. Venkatesan, S.J. Pennycook, The Atomic Circus: Small Electron Beams Spotlight Advanced Materials Down to the Atomic Scale, Adv. Mater. 30 (47) (2018) 1802402.

[14] R. Mishra, R. Ishikawa, A.R. Lupini, S.J. Pennycook, Single-atom dynamics in scanning transmission electron microscopy, MRS Bull 42 (9) (2017) 644–652.

[15] O. Dyck, C. Zhang, P.D. Rack, J.D. Fowlkes, B. Sumpter, A.R. Lupini, S.V. Kalinin, S. Jesse, Electron-beam introduction of heteroatomic Pt–Si structures in graphene, Carbon (2020).

[16] S.J. Pennycook, Z-contrast stem for materials science, Ultramicroscopy 30 (1) (1989) 58–69.

[17] S.J. Pennycook, D.E. Jenson, High-resolution Z-contrast imaging of crystals, Ultramicroscopy (1991) 14–38.

[18] P. Vincent, H. Larochelle, I. Lajoie, Y. Bengio, P.-A. Manzagol, Stacked Denoising Autoencoders: Learning Useful Representations in a Deep Network with a Local Denoising Criterion, J. Mach. Learn. Res. 11 (2010) 3371–3408.

[19] L. Gondara, Medical Image Denoising Using Convolutional Denoising Autoencoders, in: 2016 IEEE 16th International Conference on Data Mining Workshops (ICDMW), 12-15 Dec. 2016, 2016, pp. 241–246.

[20] G.A. Pavliotis, Stochastic processes and applications: diffusion processes, the Fokker-Planck and Langevin equations, 60, Springer, 2014.